Evaluation of Remote Sensing Aerial Systems in Existing Transportation Practices, Phase II

Prepared by

West Virginia University

The Pennsylvania State University ❖ University of Maryland University of Virginia ❖ Virginia Polytechnic Institute and State University ❖ West Virginia University

Evaluation of Remote Sensing Aerial Systems
In Existing Transportation Practices – Phase II

PRINCIPAL INVESTIGATOR (PI):
Yu Gu, Ph.D.,
Research Assistant Professor
Department of Mechanical and Aerospace Engineering
West Virginia University
P.O. Box 6106
Morgantown, WV 26506

Co-PIs:
David Martinelli, Ph.D.,
Marcello Napolitano, Ph.D.,
Brad Seanor, Ph.D.,
West Virginia University
Morgantown, WV 26506

PROJECT REPORT PREPARED FOR:

West Virginia Division of Highways
Capitol Complex, Building five
Charleston, WV 25305

June 2011

1. Report No. WVU-2009-01	2. Government Accession No.	3. Recipient's Catalog No.	
4. Title and Subtitle Evaluation of Remote Sensing Aerial Systems in Existing Transportation Practices, Phase II		5. Report Date June 2011	
		6. Performing Organization Code	
7. Author(s) Yu Gu, David Martinelli, Marcello Napolitano, Brad Seanor		8. Performing Organization Report No.	
9. Performing Organization Name and Address West Virginia University Morgantown, WV		10. Work Unit No. (TRAIS)	
		11. Contract or Grant No. DTRT07-G-0003	
12. Sponsoring Agency Name and Address West Virginia Department of Highways Capitol Complex, Building 5 Charleston, WV 25305 US Department of Transportation Research & Innovative Technology Admin UTC Program, RDT-30 1200 New Jersey Ave., SE Washington, DC 20590		13. Type of Report and Period Covered Final	
		14. Sponsoring Agency Code	
15. Supplementary Notes COTR: Donald Williams, WVDoH 304-677-4000			

16. Abstract

 A low-cost aerial platform represents a flexible tool for acquiring high-resolution images for ground areas of interest. The geo-referencing of objects within these images could benefit civil engineers in a variety of research areas including, but not limited to, work zone management, traffic congestion, safety, and environmental impact studies. During the Phase II effort, a Remotely Controlled (R/C) aircraft based remote sensing platform was developed and flight tested at West Virginia University (WVU). Main components of the remote-sensing payload system include a high-resolution digital still camera, a 50 Hz GPS receiver, a low-cost Inertial Navigation System (INS), a down-looking laser range finder, a custom-designed flight data recorder, and a wireless video transmission system. An extensive time-calibration and analysis effort for major measurement instruments was performed to assure that flight data were properly time-aligned. Additionally, an Unscented Kalman Filter (UKF) based 15-state GPS/INS sensor fusion algorithm was developed to estimate the aircraft attitude angles in flight. Based on the added range and orientation information for the camera, the geo-referencing software developed in Phase I effort was enhanced. The performance of the software was evaluated using a set of flight data and the known location of a fixed reference point on the ground. The flight data analysis shows an approximately 7.2 meter mean position estimation error was achieved with estimates from a single aerial image, after a set of lens distortion and the camera orientation corrections. Furthermore, a 0.5 meter position estimation error was achieved with the averaging of 15 individual estimates.

17. Key Words Aerial sensing, airborne sensors, highway data acquisition, remote sensing		18. Distribution Statement No restrictions. This document is available from the National Technical Information Service, Springfield, VA 22161	
19. Security Classif. (of this report) Unclassified	20. Security Classif. (of this page) Unclassified	21. No. of Pages	22. Price

Evaluation of Remote Sensing Aerial Systems
In Existing Transportation Practices – Phase II

Abstract

A low-cost aerial platform represents a flexible tool for acquiring high-resolution images for ground areas of interest. The geo-referencing of objects within these images could benefit civil engineers in a variety of research areas including, but not limited to, work zone management, traffic congestion, safety, and environmental impact studies. During the Phase II effort, a Remotely Controlled (R/C) aircraft based remote sensing platform was developed and flight tested at West Virginia University (WVU). Main components of the remote-sensing payload system include a high-resolution digital still camera, a 50 Hz GPS receiver, a low-cost Inertial Navigation System (INS), a down-looking laser range finder, a custom-designed flight data recorder, and a wireless video transmission system. An extensive time-calibration and analysis effort for major measurement instruments was performed to assure that flight data were properly time-aligned. Additionally, an Unscented Kalman Filter (UKF) based 15-state GPS/INS sensor fusion algorithm was developed to estimate the aircraft attitude angles in flight. Based on the added range and orientation information for the camera, the geo-referencing software developed in Phase I effort was enhanced. The performance of the software was evaluated using a set of flight data and the known location of a fixed reference point on the ground. The flight data analysis shows an approximately 7.2 meter mean position estimation error was achieved with estimates from a single aerial image, after a set of lens distortion and the camera orientation corrections. Furthermore, a 0.5 meter position estimation error was achieved with the averaging of 15 individual estimates.

Table of Contents

List of Figures

List of Tables

Evaluation of Remote Sensing Aerial Systems
In Existing Transportation Practices – Phase II

1. Introduction

Research efforts toward enhancing highway safety and improving operational efficiency strongly depend on the quality and quantity of available data. Traditional sensors such as those embedded under the pavement are routinely used for data collection by civil engineers. However, their fixed geo-locations limit their flexibility under dynamically evolving situations; additionally, increasing the number of sensors is a costly and time-consuming option. Alternatively, the proper integration of emerging technologies, such as Autonomous Systems (AS), GPS, and image processing, can today provide a complementary solution that can revolutionize highway data acquisition.

Compared to fixed-position sensors, airborne sensors mounted on small aircraft offer mobility and flexibility, and low-cost solutions for highway data acquisition [1]. For example, airborne sensors can be quickly deployed to an area of interest and provide observations from multiple perspectives. Another advantage of using small aircraft is that they are significantly lighter and have lower operational costs compared to manned aircraft, leading to substantial cost savings and reduced logistics. Small unmanned aircraft can also be used to perform missions within hazardous environments without endangering the operators. A recent mission into the eye of hurricane Ophelia by the Aerosonde aircraft [2] was a clear example of how small AS are capable of operating within a hazardous environment. The recent events at the nuclear power plant in Fukushima (Japan) also provide a clear example of a situation where the deployment of unmanned aircraft with specific payloads would provide a much safer alternative to human inspection.

The *objective* of this effort is to provide a technology demonstrations for a flexible, intelligent, and low-cost airborne data acquisition solution to complement existing highway measurement systems. The remote sensing system should be capable of providing multi-channel measurements of the transportation system on a per-need basis. Within this objective, the definition of "*flexible*" requires that the aerial platform must have the capability of carrying a variety of payloads, performing multiple functions, and operating from various locations under different weather conditions. "*Intelligent*" requires that the system shall be operated with minimum human interaction and training requirements. "*Low-cost*" requires that the completed airborne system shall have a low equipment cost, require no more than two operators with limited training, and be self-sustaining without the need for modifications to the existing DOT sensor infrastructure.

During the first year effort (Phase I), a proof-of-concept demonstration of an aerial data acquisition system was performed using one of the West Virginia University (WVU) low-cost Remotely-Controlled (R/C) aircraft, nicknamed '*Foamy*'. This platform was instrumented with a GPS receiver, a Commercial-Off-The-Shelf (COTS) flight data recorder, downlink telemetry hardware, a digital still camera, and a shutter-triggering device. With a total of 10 flights, the aircraft collected several hundred high-resolution aerial images. Geo-referencing software was

also developed in house for estimating physical distances between ground objects within an aerial image, as well as for estimating the geo-location of each ground asset of interest. A study of potential 'Sources of Error' (SOE) identified five major sources: sensor time matching error, aircraft attitude error, GPS measurement error, lens distortion, and aircraft altitude error.

During the second year effort (Phase II), the aircraft test bed was upgraded to a WVU "*Phastball-0*" platform. This platform has improved flight performance, better handling qualities, and increased payload capacity. Each of the five SOE was addressed with either hardware or software solution. Specifically, the sensor time matching error was reduced with a custom designed data logger and a set of systematic alignment procedures; the aircraft attitude angles were estimated with a GPS/INS (Global Positioning System/Inertial Navigation System) sensor fusion algorithm, which also improves the position measurements; additionally, the lens distortion was corrected in PTLens® software while the aircraft altitude error was reduced through the introduction of a laser range finder. A number of flight tests were performed with images collected in both visible spectrum and in near-Infrared. Additionally, the geo-referencing software was upgraded to incorporate the additional aircraft attitude and range information.

The rest of the report is organized as follows. Section two presents the instrumented '*Phastball-0*' test bed. Section three discusses efforts toward time-synchronization of data collected from different sensors. The GPS/INS sensor fusion algorithm is discussed in Section four. Section five describes the refinement of the geo-referencing software and presents the geo-referencing performance on the images collected through flight tests. Section six provides conclusions and outlines the follow-up research activities.

2. Airborne Data Acquisition Platform

2.1. '*Phastball-0*' Testbed

The '*Phastball-0*' airframe, showing in Figure 1, was custom developed at WVU for remote sensing research.
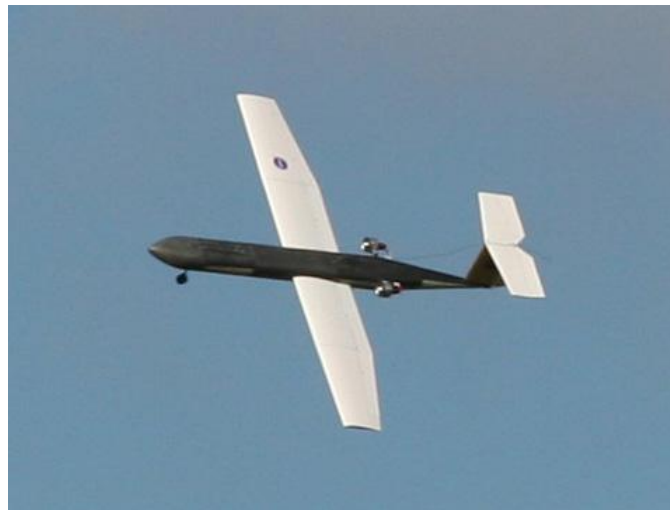
Fig. 1. 'Phastball-0' Aircraft

The airframe features a modular composite construction with most of the components manufactured in house by WVU undergraduate students. The aircraft is remotely controlled with a 9-channel R/C system and is powered with a pair of brushless electric ducted fans. The use of an electric propulsion system simplifies the flight operations and reduces the requirements for ground supporting equipment. Additionally, the low vibration generated by electric motors has a minimum impact on the quality of sensor and image data collected in flight. The aircraft features desirable handling qualities and a relatively large payload capability. The stable dynamic characteristics make this aircraft an ideal platform for remote sensing research. General specifications of the test bed aircraft are listed in Table 1:

'*Phastball-0*' Aircraft	
Length:	2.23 m (88 inch)
Wing span:	2.44 m (96 inch)
Takeoff weight:	9.5 kg (21 lbs.)
Payload capacity:	3.2 kg (7 lbs.)
Thrust:	2×25 N
T/W ratio:	0.48
Battery:	2×4900 mAh
Duration:	7 minutes
Typical turnaround:	30 minutes
Cruise speed:	25 m/s
Control channels:	L/R elevators, L/R ailerons, rudder, L/R flaps

Table 1. Aircraft General Specifications

2.2. Custom Flight Data Recorder

The COTS data logger used in Phase I research was replaced with a WVU custom designed Flight Data Recorder (FDR). The new design allowed having a full control on the sensor selection, sampling rate, data quality, and time-synchronization. The FDR along with the major components of the electronic payload is shown in Figure 2.

3.3v Regulator

IMU
(ADIS16405)

µSD Serial Recorder
(All Data excl. GPS)

4 Ch., PWM Read

3 Ch., 3.3v A/D
(3.3v pwr)

Camera Command

3 Ch., 3.3v A/D
(5v pwr)

3.3v Power LED

Programmable LED

Programmable LED

Main Power In
(6-8v)

5v Regulator

GPS Valid Fix LED

µSD Serial Recorder
(GPS Rx COM2)

Netburner COM1
(RS232)

Netburner COM-2
(RS232)

GPS Rx COM-1
(LV-TTL)

6Ch., DI/O or PWM Out

GPS Rx COM-3
(LV-TTL)

Power + SPI HUB

Netburner
(MOD5213)

ANALOG
DEVICES
ADIS16405BMLZ
0057
AD051110-4
USA 34031
1032

Fig. 2. Custom Flight Data Recorder

A Netburner MOD 5213® embedded microprocessor provides an interface between sensors, camera control, and data storage. During the flight, the FDR collects data from a GPS receiver, an Inertial Measurement Unit (IMU), a laser range finder, a photoresistor for monitoring the camera activity, as well as the pilot command from an R/C receiver. If the pilot turns on the camera activation switch on the R/C transmitter, the FDR detects this signal and sends out a sequence of camera shutter commands with a 0.5s time interval. It was experimentally determined that the camera would not respond to every shutter trigger command – resulting in issues with synchronizing the aerial images with GPS measurements. This issue was later solved; its solution is discussed in detail in Section three.

All flight data are collected with a sampling rate of 50Hz, although the laser range finder can only update at a 10Hz rate. Two Micro-SD cards are used for on-board data storage. One data card is dedicated for GPS data, which include GPS time, number of satellites used for calculating each solution, and 3-axis position and velocity in an Earth-Centered, Earth-Fixed (ECEF) frame. Another data card stores the measurements of aircraft 3-axis linear acceleration, 3-axis angular rate, 3-axis local magnetic flux, ground distance (with a laser range finder), pilot command, and camera activity. A functional block diagram of the FDR is provided in Figure 3.
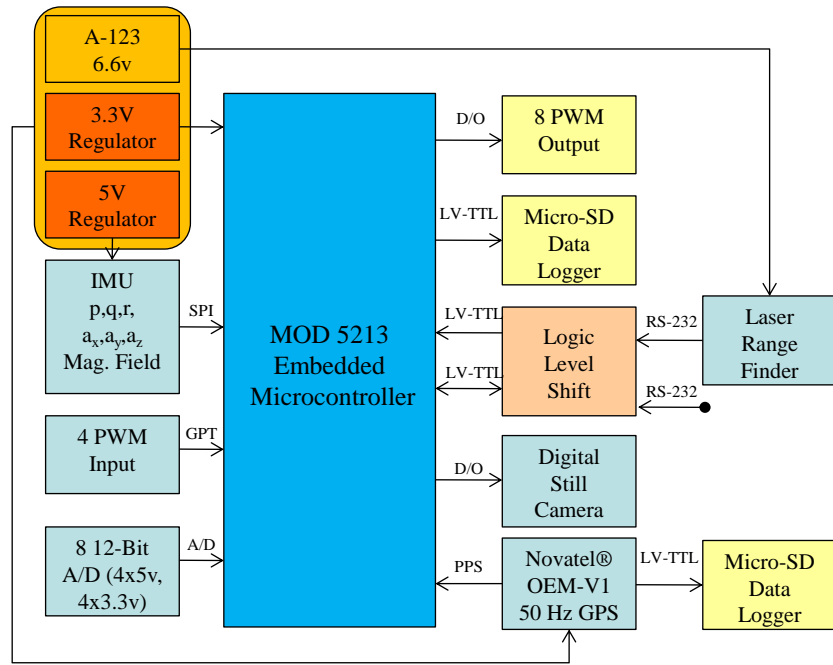
Fig. 3. Block Diagram for the Flight Data Recorder

2.3. On-board Sensors

2.3.1. Digital Still Camera

Two digital still cameras were used during this effort. The first camera is a COTS Canon Digital Rebel XTi that is mainly used for acquiring images in the visible spectrum. The second camera is a Canon Digital Rebel T1i, professionally modified to have the internal Infrared-blocking filter removed and replaced with an external Infrared-pass filter. This camera is mainly used for near-Infrared photography. Both cameras have similar dimension and weight; therefore, they are interchangeable inside the airframe and they share the same shutter triggering mechanism. Two 18-55mm lens are used in the project. They are both locked at 18mm (effective focal length 28.8mm) during flight tests. Key specifications for both cameras that are directly related to the aerial photography application are shown in Table 2.

	Canon Digital Rebel XTi	Canon Digital Rebel T1i
Max resolution	3888 x 2592	4752 x 3168
Effective pixels	10.1 million	15.1 million
Sensor size	22.2 x 14.8 mm (3.28 cm²)	22.3 x 14.9 mm (3.32 cm²)
ISO rating	100-1600	Auto, 100-3200
Max shutter	1/4000 sec	1/4000 sec
Focal length multiplier	1.6	1.6
Continuous Drive	3.0 fps, 27 JPEG	3.4 fps, 170 JPEG
Movie Clips	N/A	1920 x 1080 @ 20 fps, 1280 x 720 @ 30 fps
Remote control	E3 connector, InfraRed	E3 connector, InfraRed
Battery	720mAh Li-Ion	1050mAh Li-Ion
Weight (inc. batteries)	19.6 oz (556 g)	18.3 oz (520 g)
Dimensions	5" x 3.7" x 2.6" (127 x 94 x 65 mm)	5.1" x 3.9" x 2.4" (129 x 98 x 62 mm)

Table 2. Onboard Still Camera Specifications

8

2.3.2. GPS Receiver

A Novatel OEMV-1® GPS receiver is used to provide aircraft position, velocity, and time measurements. The GPS can be configured to have a 50Hz update rate, which provides a major advantage over the 1Hz rate provided by most GPS receivers. A list of key specifications for OEMV-1 is showing in Table 3.

OEMV-1 GPS Receiver	
Channel Configuration	14 GPS L1 1 L-band 2 SBAS
Horizontal Position Accuracy (RMS)	Single Point L1 1.5 m SBAS2 0.6 m CDGPS2 0.6 m DGPS 0.4 m
Measurement Precision (RMS)	L1 C/A Code 4 cm L1 Carrier Phase 0.5 mm
Signal Reacquisition	L1 0.5 s (typical)
Data Rate	50 Hz
Time to First Fix	Cold Start, 60s, Hot start, 35s
Time Accuracy	20 ns RMS
Velocity Accuracy	0.03 m/s RMS
Dimensions	46 x 71 x 13 mm
Weight	21.5 g
Power Consumption	1.0 W

Table 3. OEMV-1 GPS Receiver Specifications

2.3.3. Inertial Measurement Unit

An Analog Device ADIS16405 Inertial Measurement Unit (IMU) is used in the inertial navigation system, which includes a tri-axis gyroscope, a tri-axis accelerometer, and a tri-axis magnetometer in a very small package. The ADIS16405 has a temperature compensated range of −40°C to +85°C and has a digital interface. Key specifications of the ADIS16405 are listed in Table 4.

ADIS16405 Inertial Sensor	
Accelerometer Dynamic Range	± 18 g
Rate Gyroscope Dynamic Range	± 150 degree/sec
Magnetometer Dynamic Range	± 2.5 gauss
ADC resolution	14-bit
Digitally controlled sample rate	up to 819.2 SPS
Dimensions	23 x 23 x 23 mm

Table 4. Analog Device ADIS16405 Specifications

2.3.4. Laser Range Finder

An Opti-Logic RS800® laser range finder is used for measuring the distance between the on-board camera and the object in the center of the image. The use of this direct measurement could reduce the geo-referencing error due to uncertainty of the ground elevation. Key specifications of the RS800 are listed in Table 5.

RS800 Laser Range Finder	
Protocol	RS232 - 8, N, 1 (no handshaking)
Baud Rate	19200 bps
Data Raw Counts:	~200Hz
Data Calibrated Range:	~10Hz
Range:	800 Yard
Accuracy:	+/- 1m on 1x1m^2 diffuse target with 50% reflectivity
Resolution	0.2m
Dimensions	23 x 23 x 23 mm

Table 5. Opti-Logic RS800 Laser Range Finder Specifications

2.2.5. Video Camera and Transmitter

A Range video® KX171 analog video camera is installed in parallel with the digital still camera. The video is transmitted to the ground through a 900 MHz wireless link and displayed in real time with a portable TV near the pilot station. The wireless video system serves practically as a viewfinder for assisting the ground crew in determining an area of interest before taking a sequence of still images.

2.2.6. System Integration

Special attention was paid to the installation of the electronics into the '*Phastball-0*' airframe. The digital still camera, the video camera, and the laser range finder are all aligned with the aircraft x-axis. The R/C receiver antenna, GPS antenna, and the video transmitter antenna are separated to minimize any potential Electromagnetic Interference (EMI). The location of main aircraft electronic components is shown in Figure 4.

R/C Receiver
GPS Antenna
Data Logger (GPS/INS)
Laser Range Finder
Video Camera
Video Transmitter
Digital Still Camera
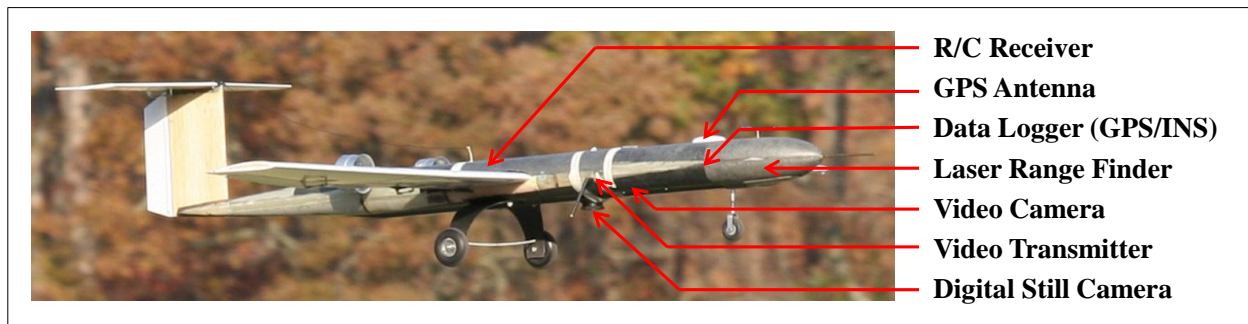
Fig. 4. 'Phastball-0' Aircraft Configuration

3. Time-Synchronization

During the Phase I study, it was determined that the time-synchronization error has a significant impact on the geo-referencing performance. As a simple example, for an aircraft flying straight and level at 25m/s, a 0.1s time matching error (five time steps in a 50Hz sampling system) between the image acquisition time and the GPS measurement point would directly translate into a 2.5m error in position estimates. During the Phase II effort, a number of experiments were designed to evaluate the time delay associated with various components of the flight instrument and the time-synchronization error was minimized with both a dedicated hardware design and a set of data analysis procedures.

In general, three major streams of flight data need to be synchronized: the GPS measurement, the aerial photos, and the remaining data collected with a Netburner embedded processor (e.g. IMU data, laser rangefinder, etc.). The alignment of these three sets of data for each flight is discussed next.

3.1. Alignment of the GPS and Netburner Data

The GPS data and the Netburner data are saved on two independent Micro-SD cards in real-time through serial ports. During the saving process some packet could get lost, thus affecting the total length of the time vector. For a 12 minute data segment, it was observed that there are, on average, 340 frames of GPS data that were lost and 145 frames of Netburner data that were lost, which translates to a 6.8s and 2.9s shorter time axis respectively. Figure 5 presents a typical packet loss pattern for the GPS and Netburner data. This figure displays the sequential difference in the recorded time, which can be used to locate lost time in the collected data. It is noted that the GPS data usually contains multiple consecutive data packet loss while the Netburner data loss pattern is more random in nature.
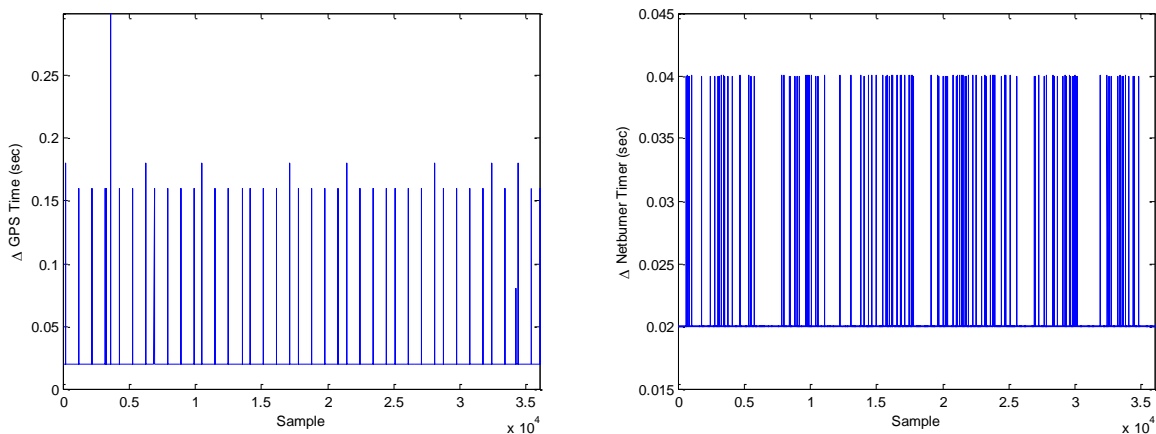
Fig. 5. GPS (left) and Netburner (right) Data Packet Loss Pattern

To restore the true time vector, an accurate time reference is needed. For the GPS data, the GPS time encoded into each data packet is used to 'stretch' the time axis back to normal. The missing packet, once detected, is replaced with a copy of the previous recorded data packet. Similarly, for the Netburner data, a counter driven by the microprocessor crystal is encoded into the header of each packet to help restoring the time axis during post-flight data analyses.

Once the time-axis's for both the GPS and Netburner data were restored, the next step was to find a correct alignment between the two. Although both the GPS and the Netburner are powered on and off at the same time during flight test operations, the simultaneous activation and de-activation do not guarantee that the data collected from both devices start and end at the same time. Due to the different amount of time required for each device to initiate, the starting time for the two data stream could differ by as much as several seconds. The ending time for the two data stream is also slightly different, depending on how much the serial data buffer was used at the time of powering off. Difference between the buffer usages of the two serial ports could

cause slightly different amounts of data loss when the system powers off. This would translate into a small difference in time (usually less than a second) for the last saved packets.

A coarse time-alignment is first performed by matching the two data streams from the end. A fine alignment is then performed with the help of a GPS PPS (Pulse Per Second) signal. A PPS is an electrical signal that precisely indicates the start of a second. It was programmed on the OEMV-1 GPS receiver to trigger a digital high at the beginning of a second and a digital low at the half of a second. This digital signal is picked up by an Analog to Digital (A/D) converter on the Netburner and is stored with other data channels. For the fine time alignment, an artificial PPS signal is constructed from the GPS data based on the time recorded in each packet. This artificial PPS signal is then compared with the measured PPS signal in the Netburner data stream. Any phase shift between the two signals is eliminated by shifting the Netburner data until a perfect time alignment is achieved. Figure 6 shows the unmatched PPS signals and the PPS signals after final alignment.
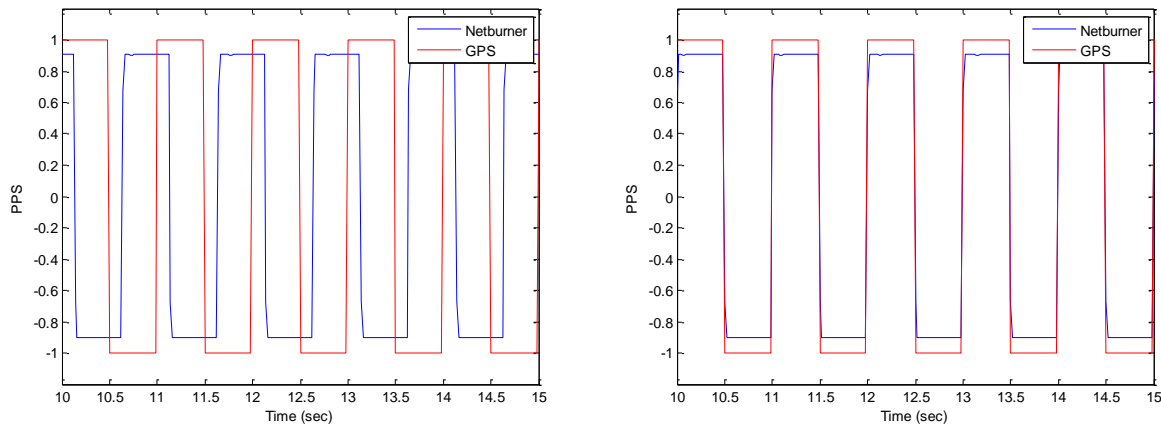
Fig. 6. PPS Signals Before (left) and After (right) the Fine Alignment

A final validation of the time-alignment performance is provided with a comparison of GPS Altitude measurement (in the GPS data stream) and the laser range finder measurement (in the Netburner data stream), as shown in Figure 7. A good time matching of the two signals indicates that a desirable time-alignment was indeed achieved.

12
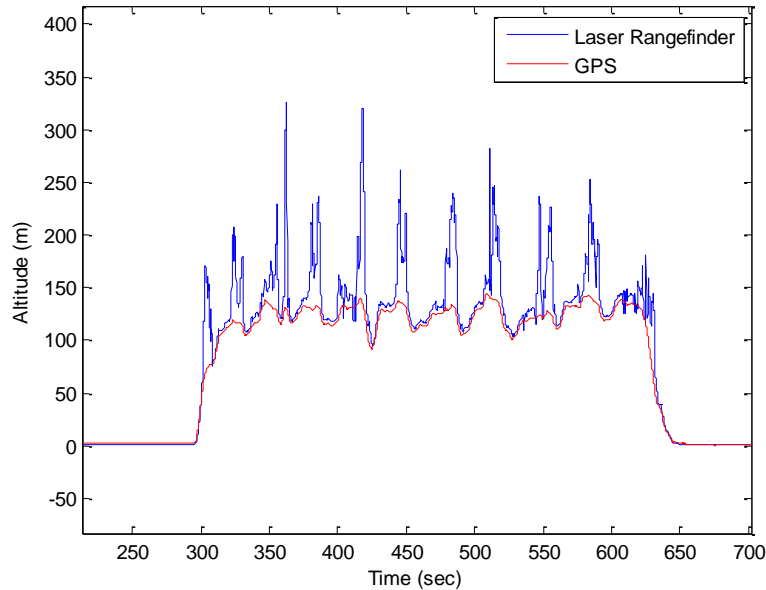
Fig. 7. A Comparison of Laser Range Finder Data and GPS Z-axis Measurement after Time-Alignment

3.2. Photo Acquisition Time

The proper matching of images or sensor data with measurements of positions where they were acquired at is one of the fundamental issues in remote sensing. Typically, this spatial alignment problem is transformed into a time matching problem, as GPS measurements are usually provided at fixed time-intervals. To achieve an accurate time alignment, it is critical to analyze the time associated with each event that happened during the data acquisition process. These events include shutter command generation, camera shutter lag, and the dynamics of any sensor used in the time measurement process.

3.2.1. Camera Shutter Lag

In photography, shutter lag is defined as the delay between the instant when the shutter is triggered and the instant when the photograph is actually recorded. This is a common problem in the photography of fast-moving objects. The term narrowly refers only to shutter effects, but more broadly refers to all lag between when the shutter button is pressed and when the photo is taken, including metering and focus lag. The latter definition is used in this report.

During a flight, the camera shutter is triggered with a digital low signal sent from the Netburner in the FDR. At the same time, a photo counter is incremented by one and is then saved with the rest of the Netburner data. It was originally planned to use this counter for synchronizing photos with remaining set of the data with the assumption that there exist a fixed shutter lag between when the shutter was triggered and when a photo was taken. To evaluate this assumption, an experiment was designed for measuring directly the shutter lag. In this experiment, the camera was remotely triggered with a radio transmitter with the same configuration as in an actual flight test. The vibration generated by the camera mirror flip and shutter movements were then measured with accelerometers in FDR, placed in close proximity to the camera. The experimental setup is shown in Figure 8.

13
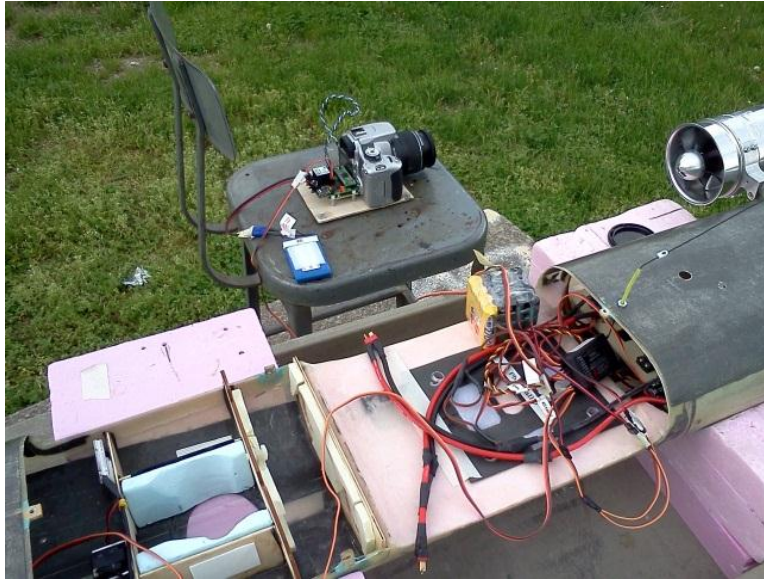
Fig. 8. Experimental Setup for Camera Shuttle Lag Measurement

The camera was set with aperture-priority at F3.5 and a sensitivity of ISO400 within a bright outdoor environment to achieve the maximum shutter speed. The 'auto focus' function was enabled and the camera was pointing at objects at a distance similar to the aircraft flying altitude. The camera shutter command, shutter counter, and vibrations picked up by an accelerometer from one of the experiments are shown in Figure 9.
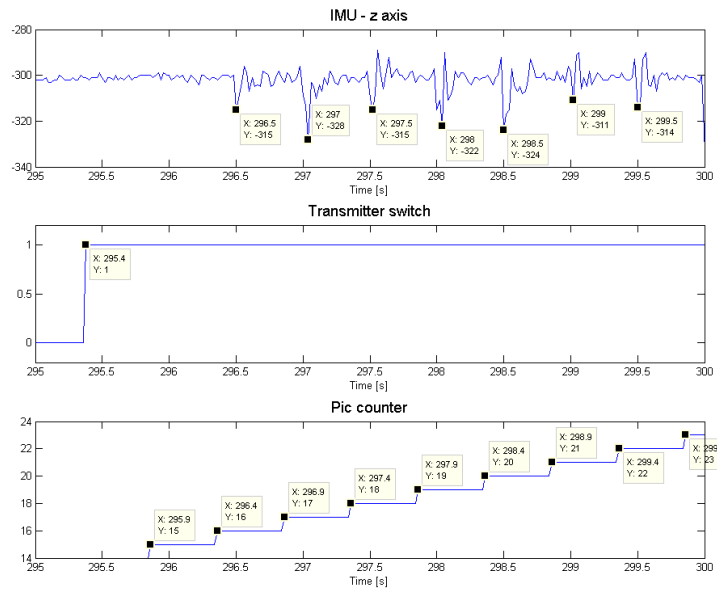
Fig. 9. Camera Shutter Vibration Measurement

With several experiments, it was determined that a delay greater than one second usually exists between the shutter switch activation and the first measured vibration. It turns out that this time delay is not constant during each individual experiment. Additionally, a typical shutter

delay for the follow up shots is approximately 0.2 second. The camera will typically stop taking any photo after 22 continuous frames, until the data buffer was cleared, although the shutter counter would continue to increase during this period.

3.2.2. Direct Shutter Activity Measurement

The shutter-lag measurement experiment concluded that the shutter counter is not a reliable indicator for the image acquisition time. With a separate experiment it was also determined that the time-stamp of each picture created by the camera is associated with the moment when the image was stored instead of when it was taken. Therefore, a direct measurement of the camera shutter activity is necessary to accurately determine the image acquisition time. It was already shown in the previous experiment that the shutter vibration can be picked up by an accelerometer in a stationary environment. However, it would be difficult to separate the shutter-induced vibration from other sources during a flight. Instead, the light intensity at the camera viewfinder for a Single Lens Reflection (SLR) camera was determined as a more reliable information source as the viewfinder would be blocked by the mirror when a photo was taken. The light intensity can be directly measured with a photoresistor attached to the camera viewfinder, as shown in Figure 10.

Fig. 10. Photoresistor Installed in a Digital SLR Rangefinder

The change in resistance of the photoresistor with a change in the light condition can be converted to a change in voltage with a simple voltage divider circuit. This signal is then measured with an A/D channel on the Netburner. Figure 11 shows the photoresistor data collected within a remote sensing flight test experiment. The spikes in the plot are associated with photos taken during the flight.

15
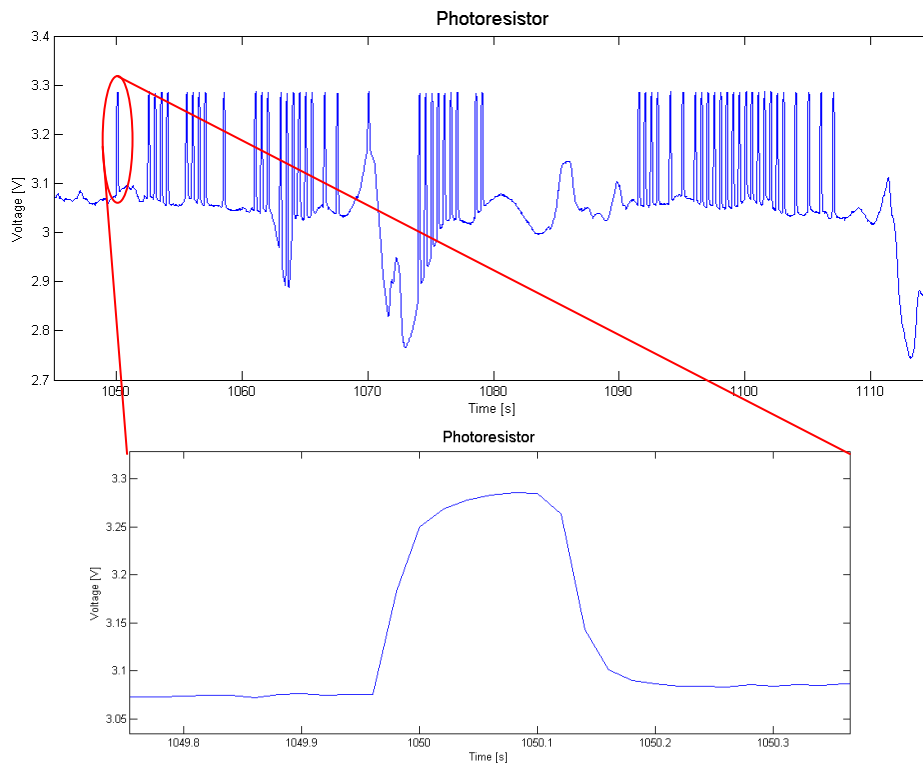
Fig. 11. Photoresistor Measurement in Flight

Following a detailed analysis of the signal, the photoresistor measurement exhibits a first-order response in both the rising and falling edges with a time constant (time it takes to reach 63% of the steady state value) approximately 0.3s. This time response is associated with both the photoresistor response time and the time it takes for the camera mirror to flip up/down. To precisely determine the actual time when a photo was taken, it is highly important to quantify pure delays associated with the photoresistor response. To achieve this goal, another experiment was designed by placing the photo resistor next to a LED on the Netburner as shown in Figure 12.
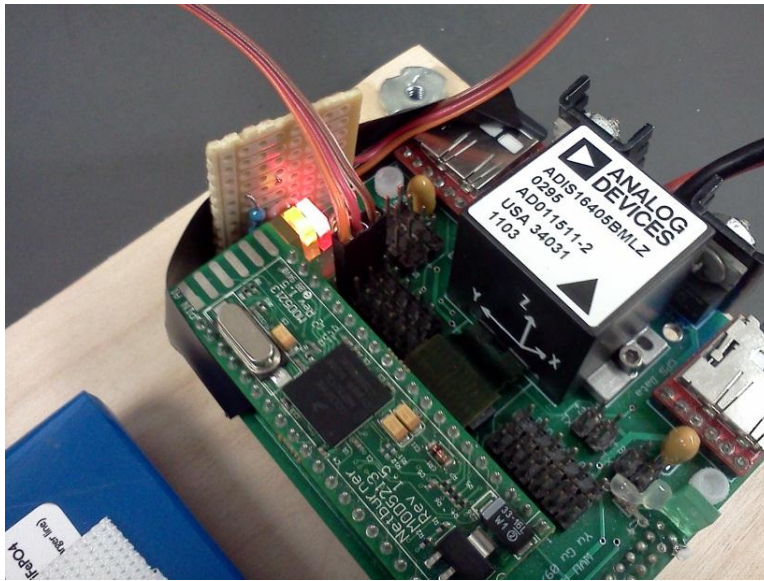
Fig. 12. Experimental Setup for Measuring the Photoresistor Time Constant

The timing of the LED was precisely controlled by the Netburner and the photoresistor measurement was also recorded. A plot showing the photoresistor response is showing in Figure 13, where the LED was turned on and off with a 2-second interval.
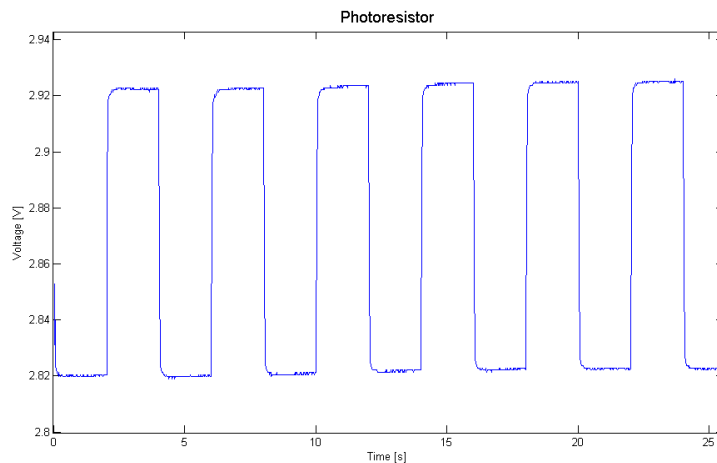
Fig. 13. Photoresistor Time Response

It is known that the transient response time of an LED is in the order of nanoseconds, the time constant of the LED is then estimated to be approximately 0.2 second with a minimum pure time delay. Due to a lack of pure delay in the photoresistor time response, it was then decided to use the time associated with the peak for each photoresistor measurement spike as an estimate of the image acquisition time. Together with the use of GPS PPS signal and direct camera shutter measurements, a systematic approach is provided to remove guesswork in the time-synchronization of the collected flight data.

4. GPS/INS Sensor Fusion

For airborne remote sensing applications, such as 3-D mapping with direct geo-referencing or constructing large image mosaics, high fidelity aircraft position and attitude information are key requirements. Recent advances of Micro-Electro-Mechanical-Systems (MEMS) technology have made low-cost Inertial Measurement Units (IMU) available; however, the limited accuracy of these components does not make them suitable for use within on-board navigation algorithms; this is mainly due to the accumulation of sensor biases over time [3]. The functional integration of a low-cost Inertial Navigation System (INS) and a Global Positioning System (GPS) receiver has well known benefits [4],[5]. The most notable advantage is that the unbiased solution offered by a GPS receiver regulates the low frequency drift associated with low-cost inertial systems, and the high frequency errors present in the GPS measurements are smoothed by inertial measurements [4].

4.1. Sensor Fusion Formulation

Most GPS/INS sensor fusion algorithms combine two information sources for attitude estimation, that is the time integration of rate gyroscopes and the known direction of the Earth's gravitational vector. In a static setting, by referencing the Cartesian components of Earth's gravitational vector, 3-axis accelerometers can be used as a tilt sensor to determine attitude [6]. However, in a dynamic environment accelerometers alone cannot distinguish between inertial and gravitational accelerations. In these situations, a GPS receiver can be used to provide information to isolate the two acceleration components, and in this sense, the GPS/accelerometers combination acts as a dynamic tilt sensor.

Within the Phase II effort, several different GPS/INS sensor fusion formulations with varying numbers of navigation states estimated and the form of GPS information used were developed and compared. The best performance was achieved with a 15-state formulation solved with a nonlinear Kalman filter, which includes 3 position states (x, y, z), three velocity states (V_x, V_y, V_z), three Attitude states (ϕ, θ, ψ), three accelerometer bias states (b_{a_x}, b_{a_y}, b_{a_z}), and three rate gyroscope bias states (b_p, b_q, b_r). Both the position and velocity states are in a local geodetic frame while the attitude states are in the aircraft body frame. The state transition equations, f, are given by:

$$\begin{bmatrix} \dot{x} \\ \dot{y} \\ \dot{z} \end{bmatrix} = \begin{bmatrix} V_x + v_{V_x} \\ V_y + v_{V_y} \\ V_z + v_{V_z} \end{bmatrix} \tag{1}$$

$$\begin{bmatrix} \dot{V}_x \\ \dot{V}_y \\ \dot{V}_z \end{bmatrix} = \begin{bmatrix} c\psi\, c\theta(a_x - b_{a_x}) + (-s\psi\, c\phi + c\psi\, s\theta\, s\phi)(a_y - b_{a_y}) + (s\psi\, s\phi + c\psi\, s\theta\, c\phi)(a_z - b_{a_z}) \\ s\psi\, c\theta(a_x - b_{a_x}) + (c\psi\, c\phi + s\psi\, s\theta\, s\phi)(a_y - b_{a_y}) + (-c\psi\, s\phi + s\psi\, s\theta\, c\phi)(a_z - b_{a_z}) \\ -s\theta(a_x - b_{a_x}) + c\theta\, s\phi(a_y - b_{a_y}) + c\theta\, c\phi(a_z - b_{a_z}) - g \end{bmatrix} \tag{2}$$

$$\begin{bmatrix} \dot{\phi} \\ \dot{\theta} \\ \dot{\psi} \end{bmatrix} = \begin{bmatrix} (p - b_p) + (q - b_q)\sin\phi\tan\theta + (r - b_r)\cos\phi\tan\theta \\ (q - b_q)\cos\phi - (r - b_r)\sin\phi \\ \left((q - b_q)\sin\phi + (r - b_r)\cos\phi\right)\sec\theta \end{bmatrix} \tag{3}$$

18

$$\begin{bmatrix} \dot{b}_{a_x} \\ \dot{b}_{a_y} \\ \dot{b}_{a_z} \\ \dot{b}_p \\ \dot{b}_q \\ \dot{b}_r \end{bmatrix} = \begin{bmatrix} v_{a_x} \\ v_{a_y} \\ v_{a_z} \\ v_p \\ v_q \\ v_r \end{bmatrix} \qquad (4)$$

, where v is random noise which is assumed to be white and Gaussian. Eq (1) and (3) are the well-known strap-down inertial navigation equations while eq. (2) transforms the acceleration measurements from the aircraft body frame to the local geodetic frame with a Direction Cosine Matrix (DCM). Eq (4) is based on a random walk model [7] for the accelerometer and rate gyro biases.

The observation matrix of the 15-state formulation is given by:

$$H = [I_{6\times6} \quad 0_{6\times9}] \qquad (5)$$

The above matrix extracts the predicted position and velocity states that are directly comparable with the GPS measured position and velocity: $\mathbf{z} = \begin{bmatrix} x_{GPS} & y_{GPS} & z_{GPS} & V_{x_{GPS}} & V_{y_{GPS}} & V_{z_{GPS}} \end{bmatrix}^T$.

4.2. Unscented Kalman Filter

The nonlinearities associated with eqs (2) and (3) require the use of a non-linear estimator [13], [15], [16] in a GPS/INS sensor fusion algorithm, to combine the information in a predictor-corrector framework. The Unscented Kalman Filter (UKF) [8] is selected in this study due to its flexibility in handling non-additive process noises.

UKF uses the Unscented Transformation (UT) to transform statistical information through non-linear functions [8]. The UKF prediction stage starts with the augmentation of the state vector with the process noise $\mathbf{x}^a = \begin{bmatrix} \mathbf{x}^T & v^T \end{bmatrix}^T$. The mean and error covariance matrix for the augmented state vector is given as:

$$\overline{\mathbf{x}}^a_{k-1|k-1} = \begin{bmatrix} \mathbf{x}^T_{k-1|k-1} & 0 \end{bmatrix}^T, P^a_{k-1|k-1} = \begin{bmatrix} P_{k-1|k-1} & 0 \\ 0 & Q \end{bmatrix} \qquad (6)$$

, which are then used to generate a set of sigma-points,

$$\chi_{k-1|k-1} = \begin{bmatrix} \overline{\mathbf{x}}^a_{k-1|k-1} & \overline{\mathbf{x}}^a_{k-1|k-1} + \lambda\sqrt{P^a_{k-1|k-1}} & \overline{\mathbf{x}}^a_{k-1|k-1} - \lambda\sqrt{P^a_{k-1|k-1}} \end{bmatrix} \qquad (7)$$

, where λ is a scaling parameter. Next, each of the sigma-points is transformed through non-linear state transition functions:

$$\chi^{i=0:2L}_{k|k-1} = f(\chi^{i=0:2L}_{k-1|k-1}, \mathbf{u}_k) \qquad (8)$$

, where L is the dimension of the augmented state vector. With the transformed sigma-points, the predicted mean and error covariance are calculated as weighted sums using:

$$x_{k|k-1} = \sum_{i=0}^{2L} w_i^m \chi^i_{k|k-1} \qquad (9)$$

$$P_{k|k-1} = \sum_{i=0}^{2L} w_i^C (\chi_{k|k-1}^i - x_{k|k-1})(\chi_{k|k-1}^i - x_{k|k-1})^T \tag{10}$$

Details on how to assign weights and scaling parameters for a UKF can be found in [9].

During a UKF measurement-update, the state vector is augmented with the measurement noise $\mathbf{x}^a = \begin{bmatrix} \mathbf{x}^T & n^T \end{bmatrix}^T$, and the predicted mean from eq. (9) and covariance from eq. (10) are used to generate a new set of sigma-points:

$$\bar{\mathbf{x}}_{k|k-1}^a = \begin{bmatrix} \mathbf{x}_{k|k-1}^T & 0 \end{bmatrix}^T \quad , P_{k|k-1}^a = \begin{bmatrix} P_{k|k-1} & 0 \\ 0 & R \end{bmatrix} \tag{11}$$

$$\chi_{k|k-1} = \begin{bmatrix} \bar{\mathbf{x}}_{k|k-1}^a & \bar{\mathbf{x}}_{k|k-1}^a + \lambda\sqrt{P_{k|k-1}} & \bar{\mathbf{x}}_{k|k-1}^a - \lambda\sqrt{P_{k|k-1}} \end{bmatrix} \tag{12}$$

which are then transformed through nonlinear observation functions:

$$Y_k^{i=0:2M} = h(\chi_{k|k-1}^i, \mathbf{d}_k) \tag{13}$$

, where M is the dimension of the augmented state vector. Subsequently, the outputs, the observation error covariance, and the cross-covariance of the predicted states and observations are calculated as weighted sums of the transformed sigma-points:

$$y_k = \sum_{i=0}^{2M} w_i^m Y_{k|k-1}^i \tag{14}$$

$$P_{\mathbf{yy}} = \left(\sum_{i=o}^{2M} w_i^C (Y_k^i - \mathbf{y}_k)(Y_k^i - \mathbf{y}_k)^T \right) \tag{15}$$

$$P_{\mathbf{xy}} = \left(\sum_{i=o}^{2M} w_i^C (\chi_{k|k-1}^i - \mathbf{x}_{k|k-1})(Y_k^i - \mathbf{y}_k)^T \right) \tag{16}$$

Finally, the UKF Kalman gain is calculated using:

$$K_k = P_{\mathbf{xy}} P_{\mathbf{yy}}^{-1} \tag{17}$$

The above gains are then used to update the predicted states and error covariance:

$$\mathbf{x}_{k|k} = \mathbf{x}_{k|k-1} + K_k(\mathbf{z}_k - \mathbf{y}_k) \tag{18}$$

$$P_{k|k} = P_{k|k-1} - K_k P_{\mathbf{yy}} K_k^T \tag{19}$$

4.3. Tuning and Estimation Performance

The attitude estimation performance was tuned and evaluated with flight data collected with the WVU "*Red-Phastball*" aircraft, which features a similar airframe and propulsion system, and identical GPS and IMU sensors. In addition, the "*Red-Phastball*" carries a high-quality Goodrich VG34® mechanical vertical gyroscope, which provides independent pitch and roll angle measurements that can be compared with the GPS/INS attitude estimates. The VG34, as shown in Figure 14, has a ±90° measurement range on the roll axis and a ±60° range on the pitch axis. It has a self-erection system, and a reported accuracy of within 0.25° of true vertical. The output of the mechanical vertical gyroscope was used as the 'truth data' for the sensor fusion study.

Fig. 14. VG34 Mechanical Vertical Gyro Scope

The attitude estimation result with the 15-state UKF sensor fusion algorithm shows a typical 2.6 degree roll standard deviation error and a 2.1 degree pitch standard deviation error. A comparison of the estimated aircraft roll angle versus the independent vertical gyro measurement is provided in Figure 15.
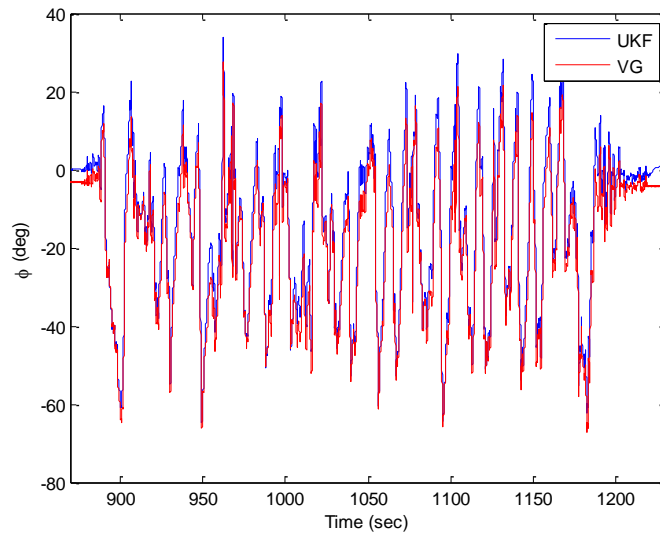
Fig. 15. Comparison of the Vertical Gyro Roll Measurement
and the GPS/INS Sensor Fusion Estimates

5. Flight Test Result and Geo-Referencing Performance

A total of eight flight tests were performed during the Phase II effort to evaluate the functionality and performance of the airborne image/data acquisition system. The typical flight path has a NASCAR loop pattern including two straight legs and two turns. Images were normally taken during the straight leg section and over the areas of interest. Typically, approximately 150-200 photos were taken during each flight. Figure 16 shows two sample images of the same general region with both visible and near-IR wavelengths.

Fig. 16. Aerial Photos of the Same Region with Visible Spectrum and Near-IR

5.1. Reference Position

To quantify the geo-referencing performance, a fire hydrant located in the airfield was selected as a reference position. An aerial photo of the fire hydrant and the GPS setup is shown in Figure 17.

Fig. 17. The Reference Location

The location of the fire hydrant was continuously measured with a GPS receiver for 5.5 hours at a 20Hz update rate. An average of a total 396,000 measurements was then used to

estimate the location of the fire hydrant. Figure 18 shows the distribution of the measurements, their mean, and the 1-σ (65%) confidence interval.
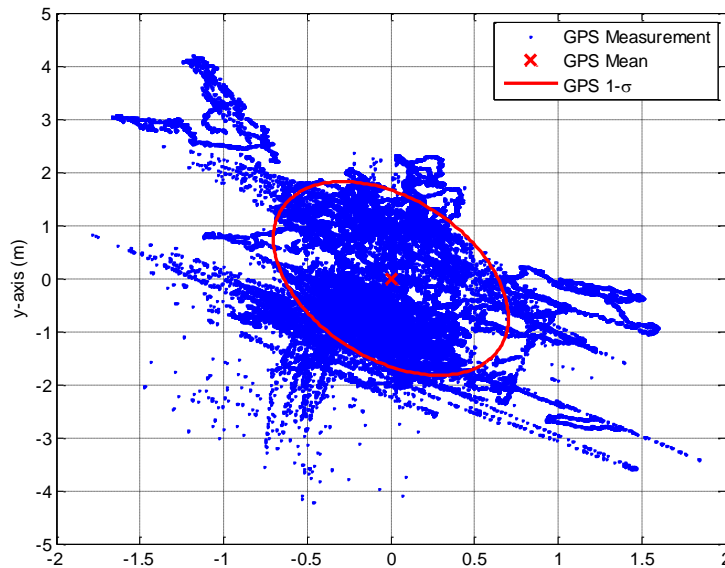

Fig. 18. Distribution of the GPS Measurements for the Reference Location

Figure 18 confirms the performance of the manufacturer reported performance of the GPS receiver and also indicates that under worst case condition a single GPS measurement could have up to 5 meter horizontal error.

5.2. Geo-Reference Procedures

The process of geo-referencing is based on the knowledge of the camera states when an image was taken, which include the focal length of the lens, the dimensions of the CCD/CMOS sensor in the camera, the position and orientation of the camera, and the distance between the camera and the object of interest. A simple formula describes the relationship between the focal length of a lens, the sensor size, the distance of a subject and the field of view that is covered by the image:

$$\rho = H\frac{\tau}{f} \tag{20}$$

where ρ is the field of view of the camera (in meters), H is the distance from the camera to the object in the center of the photo (in meters), τ is the physical dimension of the camera sensor and f is the focal length of the lens, in millimeters. The physical sizes of objects in the photo can then be determined using a conversion factor ξ between pixels and meters:

$$\xi = \frac{\rho}{\chi} \tag{21}$$

where is χ is the total number of pixels along the direction of ρ in the image.

Within a remote sensing application the estimated physical sizes and location must also be correlated to a standard coordinate system, such as the common LLA (Latitude-Longitude-Altitude) coordinate system. The relationship between a distance in meters and the relative

23

difference in terms of Latitude-Longitude is calculated assuming the WGS 84 ellipsoid model for the Earth shape, thus a distance in meters corresponds to a change in degrees of:

$$\delta = \frac{d}{v} \tag{22}$$

where δ is the variation of longitude or latitude in degrees, d is the distance in meters and v is the length in meters of a degree of arc for either latitude or longitude, that is calculated using the basic information of the earth ellipsoid. While the length of the longitudinal arc is constant at all longitudes, the length of the latitudinal arc needs to be adjusted for different latitudes.

During a remote sensing operation, the latitude and longitude of the object in the image center usually does not overlap with the coordinate of the camera. This is due to the attitude angles of the aircraft at the instant of the picture, since the aircraft is not always flying wings level. The coordinate of the image center can be estimated using the attitude angles provided by the GPS/INS sensor fusion algorithm. Specifically, the attitude angles are used to transform the components of the vertical vector of the airplane from the local body-axes system to the LLA.

$$G_v = \begin{bmatrix} G_{v\_Lat} \\ G_{v\_Lon} \\ G_{v\_Alt} \end{bmatrix} = \begin{bmatrix} \cos\theta\cos\psi & \sin\phi\sin\theta\cos\psi - \cos\phi\sin\psi & \cos\phi\sin\theta\cos\psi + \sin\phi\sin\psi \\ \cos\theta\sin\psi & \sin\phi\sin\theta\sin\psi + \cos\phi\cos\psi & \cos\phi\sin\theta\sin\psi - \sin\phi\cos\psi \\ -\sin\theta & \sin\phi\cos\theta & \cos\phi\cos\theta \end{bmatrix} \begin{bmatrix} 0 \\ 0 \\ 1 \end{bmatrix} \tag{23}$$

The angular deviation of the aircraft z axis from the altitude axis in the LLA frame can be captured with two angles:

$$\eta = \arctan\left(\frac{G_{v\_Alt}}{G_{v\_Lat}}\right)$$

$$\lambda = \arctan\left(\frac{G_{v\_Alt}}{G_{v\_Lon}}\right) \tag{24}$$

If the local ground elevation information is available and assuming a flat ground, the position correction for the image center along the latitude and longitude axis can be calculated with:

$$\begin{cases} \Delta Lat = H\tan\eta \\ \Delta Lon = H\tan\lambda \end{cases} \tag{25}$$

If the elevation information is unavailable, the laser range finder measurement can be used as the distance between the camera and the object in the image center. The coordinate correction terms can then be calculated with:

$$\begin{cases} \Delta Lat = H\sin\eta \\ \Delta Lon = H\sin\lambda \end{cases} \tag{26}$$

With the corrected position for the image center, the geo-referencing performance for other objects in the image can also be improved.

5.3. Geo-Referencing Results

A detailed geo-referencing performance analysis was performed on the May 27th 2011 Flight #1. A total of 175 visible-spectrum images were collected during the six-minute flight. After scanning through all the images, 15 photos containing the fire hydrant reference point were selected for quantifying the geo-referencing performance. To represent a realistic remote sensing operation scenario, each photo was taken in the straight legs of the flight path and the R/C

ground pilot was trying to keep the aircraft as level as possible. As a result, the mean pitch and roll angles for the 15 photos were 1.93° and 2.44° respectively, according to the GPS/INS sensor fusion algorithm. The mean aircraft flight altitude and ground speed were 113.4 m and 26.5 m/s respectively. The camera field of view at a distance of 110 meter is 135.7 × 90.4 meters. The result of a detailed geo-referencing study is presented in Table 6 in Appendix 1. The position estimation was first performed with a perfect knowledge of the reference point altitude, and is processed with raw flight data, lens distortion removal, and aircraft attitude correction respectively. It was noticed that the lens distortion removal had a minimum influence on the estimation performance in this study. The mean and standard deviation position estimation error were approximately 12.6 m and 6.7 m respectively after the distortion removal. The use of the GPS/INS attitude correction greatly reduced the geo-referencing error, leading to a 7.2 m (43% reduction) mean error and a 3.2 m (52% reduction) standard deviation error. Note that this large error reduction is achieved with only very small attitude angles. If the angles are larger during the flight a higher percentage error reduction could be achieved, as evidenced in Table 6 with the last three images. Additionally, the position estimates from individual images are randomly distributed around the true value, as shown in Figure 19.
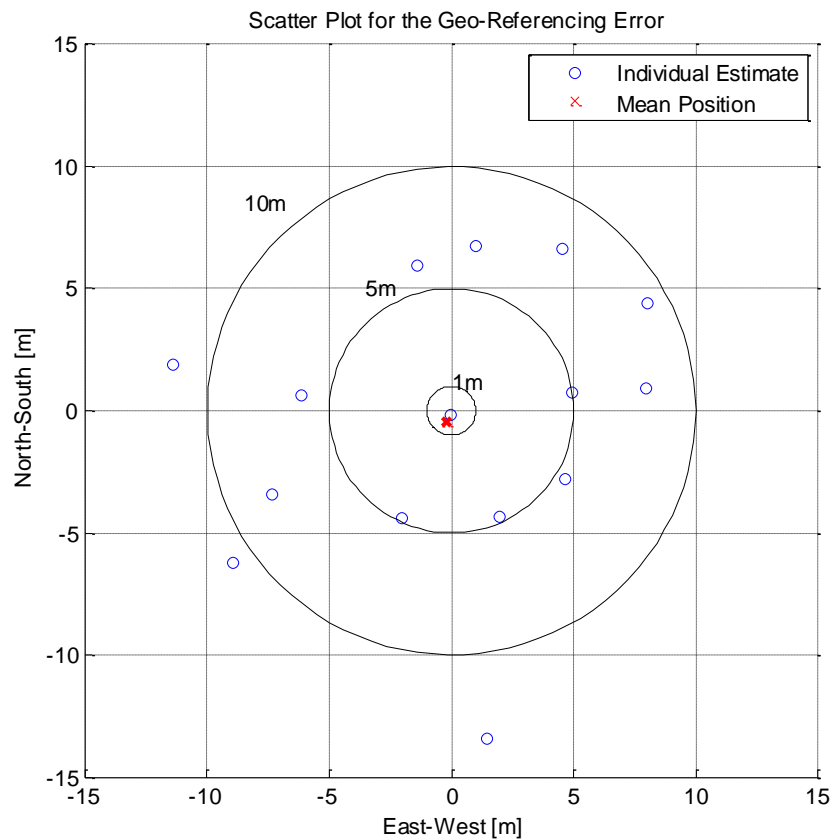
Fig. 19. Distribution of the 15 Position Estimates

Figure 19 shows that although individual estimates have a 7.2 m mean error, a simple action of averaging multiple measurements could significantly reduce the geo-referencing error. In this case, an average of 15 measurements reduced the position estimation error to 0.5 m, which is lower than the typical error for a single direct GPS measurement at the site.

If the ground elevation data was not available, the laser range finder data could be used for measuring the distance between the camera and the image center. The associated geo-referencing result is also listed in Table 6 in the last three columns, with a slightly increased position estimation error (8.7 m for the mean error and 4.1 meter for the standard deviation error) compared to the case with the perfect altitude knowledge. Again, an average of 15 measurements provides a 1.4 m total position estimation error.

6. Conclusions

The mountainous terrain of West Virginia provides several unique challenges for highway management, especially under emergency situations such as flooding or forest fire. The development of a 'standalone' remote sensing system could provide an alternative method for collecting highway data that would be otherwise difficult to acquire with traditional methods. The low cost and flexibility characteristic of a small remote control aircraft also enables rapid response, allowing first-hand information to be collected on a timely basis during an emergency situation. Within the Phase II effort, the airborne data acquisition system has been refined and reached a substantially higher level of maturity. The successful completion of the Phase II effort demonstrated that a low cost aerial platform with a proper alignment and fusion of flight data can achieve a high-level of geo-referencing performance. The extraction of accurate information from these images would benefit civil engineers in a variety of research areas including, but not limited to, work zone management, traffic congestion, safety, and environmental impact.

The activities of this project also provided excellent opportunities for students to perform hands on research, and increase their exposure to the latest technology in sensors, electronics, image processing, sensor fusion, software development, and flight-testing. During the Phase II effort, five graduates and one undergraduate student were involved. The undergraduate student contributed to the '*Phastball-0*' aircraft construction and maintenance. Two graduate students were involved into the sensor fusion algorithm development; one graduate student contributed to the geo-referencing software, while two graduate students contributed to the testing and calibration of individual components. Students involved with this research have acquired hands-on experience as a preparation for their professional careers.

Throughout this effort, valuable experience has been acquired on how to instrument and calibrate an aerial platform for geo-referencing purposes. Future work would focus on continuing refining the sensor system and post-processing software, leading to an improved position estimation performance. Particularly, a comprehensive study of how random errors propagate through nonlinear equations during the geo-referencing process would provide more insight on how many measurements would be needed to achieve a desired level of geo-referencing accuracy. Additional work will also focus on miniaturizing the aircraft payload system and improve the user-friendliness of the airborne data acquisition system, so that it can be operated by highway researchers with a minimum training requirement.

References

[1] Puri, A., *A Survey of Unmanned Aerial Vehicles (UAV) for Traffic Surveillance*, Available: www.csee.usf.edu/~apuri/techreport.pdf

[2] Aerosonde, *Aerosonde first UAV to Recce a Tropical Cyclone*, Available: http://www.aerosonde.com/ drawarticle/127

[3] El-Diasty, M. and Pagiatakis, S., "A Rigirous Temperature-Dependent Stochastic Modelling and Testing for MEMS-Based Inertial Sensor Errors." Sesnors 2009, s.l. : MDPI, 2009, Vol. 9, pp. 8473-8489. ISSN 1324-8220.

[4] Grewal, M. S., Weill, L. R and Andrew, A.P., *Global Positioning, Inetial Navigation & Integration.* 2nd. New York, NY : John Wiley & Sons, 2007.

[5] Kaplan, E. and Heagarty, C., *Understanding GPS Principles and Applications.* 2nd. Norwood, MA : Arttech House, 2006.

[6] Łuczak, S., Oleksiuk, W. and Bodnicki, M., "Sensing Tilt With MEMS Accelerometers." IEEE Sensors, December 2006, Issue 6, Vol. 6, pp. 1669-1673.

[7] El-Diasty, M. and Pagiatakis., "Calibration and Stochastic Modelling of Inertial Navigation Sensor Errors." Journal of Global Positioning Systems, s.l. : CPGPS, 2008, Issue 2, Vol. 7, pp. 170-182.

[8] Wan, E. and van der Merwe, R., "The Unscented Kalman Filter for Nonlinear Estimation." Lake Loise, Alberta, CA : s.n., 2000. Proceedings of IEEE 2000 AS-SPCC Symposium.

[9] van der Merwe, R., Wan, E. and Julier, S., "Sigma-Point Kalman Filters for Nonlinear Estimation and Sensor Fusion- Applications to Integrated Navigation." Providence, RI : AIAA, 2004. AIAA Guidance, Navigation and Control Conference. 2004-5120.

Appendix 1. Geo-Referencing Results

Image Name	Aircraft Euler Angles (degree)*			Laser Range Finder (m)	Ground Speed (m/s)	Distance to Image-center (m)†		Position Estimation Error with Raw Data (m)			Error w/ (Distortion Removal) (m)‡			Error w/ (Distortion +Attitude Correction) (m)			Error without Ground Elevation Information (m)§		
	Pitch	Roll	Yaw	(m)		Lat	Lon	Lat	Lon	Total	Lat	Lon	Total	Lat	Lon	Total	Lat	Lon	Total
IMG 7242	-0.66	3.72	223.52	114.68	26.43	36.34	37.21	-5.43	6.52	8.48	-6.06	5.81	8.40	-1.42	5.96	6.13	-5.17	4.40	6.79
IMG 7243	0.23	3.82	223.07	114.10	24.31	36.43	23.96	8.03	8.29	11.54	8.48	8.05	11.69	1.00	6.77	6.84	1.99	6.90	7.18
IMG 7244	3.14	4.19	289.88	114.34	26.57	34.71	15.59	0.26	3.13	3.15	0.33	3.27	3.29	-0.02	-0.15	0.15	-1.46	-1.15	1.86
IMG 7245	2.19	1.77	265.21	114.10	26.48	35.16	2.48	3.04	0.72	3.12	2.67	0.62	2.74	4.94	0.73	4.99	-3.78	17.59	17.99
IMG 7246	3.11	5.98	194.08	114.68	25.85	34.19	28.57	-9.48	1.41	9.59	-9.17	1.40	9.27	1.97	-4.36	4.79	1.12	-3.71	3.87
IMG 7247	3.27	4.92	237.93	115.37	25.58	33.49	41.41	-15.88	-10.48	19.02	-16.28	-10.68	19.47	-7.37	-3.40	8.12	-8.53	-2.26	8.82
IMG 7268	2.93	-2.87	344.51	115.26	24.41	27.65	38.29	17.22	0.66	17.24	17.27	1.01	17.30	7.96	0.90	8.01	10.95	-6.76	12.87
IMG 7269	2.91	-2.10	330.46	115.54	24.23	26.09	26.25	11.66	0.78	11.69	11.89	1.15	11.95	8.03	4.41	9.17	7.02	-5.55	8.95
IMG 7270	0.58	-1.99	329.69	115.37	24.02	24.72	14.27	8.83	-3.85	9.63	8.78	-3.32	9.38	4.68	-2.77	5.44	4.06	-5.11	6.53
IMG 7271	0.81	-0.07	286.81	114.45	24.06	23.50	2.30	4.01	7.77	8.75	4.53	7.98	9.17	4.51	6.65	8.04	3.75	6.60	7.59
IMG 7272	0.01	0.93	260.05	113.47	24.16	22.44	9.22	-0.67	-13.27	13.29	-0.22	-13.31	13.32	1.47	-13.45	13.53	0.38	-13.56	13.56
IMG 7273	0.33	-0.19	235.24	113.31	24.31	21.38	21.76	-2.90	-4.90	5.70	-2.51	-5.21	5.79	-2.04	-4.39	4.84	-2.98	-4.15	5.11
IMG 7274	-0.75	8.67	229.67	113.02	42.41	19.37	45.60	-24.61	-8.26	25.96	-25.62	-7.69	26.75	-8.93	-6.23	10.88	-9.55	-5.60	11.07
IMG 7307	5.17	5.98	348.43	105.78	27.16	11.75	14.28	-16.52	9.41	19.01	-16.60	9.82	19.29	-6.14	0.64	6.17	-5.62	1.37	5.79
IMG 7308	5.63	3.82	354.70	107.39	26.70	14.54	27.39	-18.13	12.08	21.79	-18.19	11.96	21.77	-11.42	1.89	11.57	-11.28	3.50	11.81
Mean	1.93	2.44	-	113.39	26.45	26.78	23.24	-2.70	0.67	12.53	-2.71	0.72	12.64	-0.18	-0.45	7.24	-1.27	-0.50	8.65
Standard Deviation	1.95	3.30	-	2.79	4.41	7.80	13.15	11.77	7.33	6.56	12.00	7.29	6.74	5.83	5.32	3.16	6.09	7.24	4.05

Table 6. Data Analysis for May 27th 2011 Flight Test #1

---

* Estimated with the 15-state UKF GPS/INS sensor fusion algorithm;

† An indication of how far is the object from the image center in a photo; It shows that in most images, the reference object is actually away from the center;

‡ Image distortion removed in software;

§ Using laser range finder instead of the known altitude of the object in the geo-referencing algorithm.